PAPER

Check for updates

PTX-loaded Fe₃O₄@polydopamine nanoparticle complexes for antitumor therapy cell carcinoma: synergistic chemotherapy and *in vivo* efficacy

Jie Zhang,†[a] Qinkun Jiang,†[ab] Zichen Xu,†[a] Zhiliang Nie,[a] Runying Guo,[a] Yang Liu,[a] Xinjian Zhang,[a] Wei Li[a] and Jiaxuan Qiu ⓘD *[a]

Oral squamous cell carcinoma (OSCC) stands as one of the most prevalent malignant neoplasms in the head and neck region, with tongue squamous cell carcinoma (TSCC) emerging as the most frequent subtype. The management of advanced TSCC typically encompasses chemotherapy, surgery, radiotherapy, or a combination thereof. Nonetheless, conventional chemotherapeutic agents are often characterized by their cytotoxicity, lack of specificity, and potential to induce tumor drug resistance. In recent years, advancements in nanotechnology have led to the emergence of targeted nano-drug delivery systems as a pivotal area of pharmaceutical research, garnering considerable attention owing to their potential in cancer treatment. This study is dedicated to the development of polydopamine-coated Fe₃O₄ nanoparticles (Fe₃O₄@PDA NPs) designed to facilitate precise, targeted anti-tumor chemotherapy, enhance the cytotoxic efficacy of chemotherapeutic agents against tumor cells, and ultimately inhibit tumor progression. The particle size of Fe₃O₄@PDA−PEG−PTX NPs was approximately 190 nm. *In vivo* cell experiments demonstrated that Fe₃O₄@PDA−PEG−PTX NPs exhibited good biocompatibility and biosafety, effectively killing tongue squamous carcinoma tumor cells. The results of *in vivo* and *in vitro* experiments using nude mice revealed that Fe₃O₄@PDA−PEG−PTX NPs exerted a stronger tumor inhibitory effect compared to free PTX. Furthermore, under the influence of an external magnetic field, Fe₃O₄@PDA−PEG−PTX NPs significantly inhibited tumor growth and demonstrated a pronounced anti-tumor effect *in vivo*, thus achieving the goal of precise targeted therapy. In summary, Fe₃O₄@PDA−PEG−PTX NPs exhibit a significant anti-tumor effect on oral tongue squamous cell carcinoma and demonstrate enhanced tumor inhibition ability under the influence of an external magnetic field. This confirms that the use of Fe₃O₄@PDA−PEG−PTX NPs for cancer treatment achieves the effect of precise targeted therapy and holds potential for improving therapeutic efficacy. These findings indicate that Fe₃O₄@PDA−PEG−PTX NPs possess considerable potential and prospects for further development in clinical applications.

1. Introduction

Oral squamous cell carcinoma (OSCC), a predominant malignancy in the head and neck region, is clinically characterized by aggressive proliferation and frequent invasion. Among OSCC subtypes, tongue squamous cell carcinoma (TSCC) constitutes the most prevalent histological form.[1] Current therapeutic modalities for TSCC encompass surgical resection, radiotherapy, chemotherapy, or combined modality approaches.[2–4] Nevertheless, conventional chemotherapy often induces systemic adverse effects including gastrointestinal disturbances, myelosuppression, and hepatorenal toxicity, while also leading to chemoresistance development—factors that collectively compromise therapeutic outcomes.[5] Surgical interventions, though essential for tumor eradication, frequently impair postoperative quality of life due to the anatomical and functional complexity of oral structures. These limitations underscore the clinical imperative to develop novel therapeutic strategies integrating chemotherapeutic optimization with targeted delivery systems, aiming to enhance treatment efficacy while minimizing off-target effects.

Paclitaxel (PTX), a tricyclic diterpenoid derived from *Taxus* species bark,[6] has emerged as a first-line chemotherapeutic agent through its unique microtubule-stabilizing mechanism.[7,8]

[a] Jiangxi Provincial Key Laboratory of Oral Diseases, Department of Stomatology, The First Affiliated Hospital, Jiangxi Medical College, Nanchang University, Nanchang, Jiangxi, 330006, China. E-mail: xqiujiaxuan@163.com; Tel: +86-13870613188

[b] Postdoctoral Innovation Practice Base, The First Affiliated Hospital, Jiangxi Medical College, Nanchang University, Nanchang, China

† These authors contributed equally to this work and share first authorship.

Despite proven efficacy in diverse malignancies including hepatocellular carcinoma, breast cancer, and non-small cell lung cancer,[9] PTX application in OSCC management—primarily as adjuvant therapy for advanced stages—faces three critical challenges: (1) inherent hydrophobicity necessitating elevated dosing due to poor aqueous solubility;[10] (2) development of multidrug resistance mechanisms shared with other cytotoxics; (3) suboptimal tumor specificity resulting in off-target biodistribution.[11] These pharmacological constraints, compounded by rapid systemic clearance and limited bioavailability,[12,13] severely restrict its clinical utility in oral oncology. Thus, engineering innovative drug delivery platforms to overcome these barriers remains an unmet clinical need.

Recent advances in nanomedicine have propelled the development of targeted drug delivery systems (TDDS) capable of enhancing tumor-specific drug accumulation through enhanced permeability and retention (EPR) effects while minimizing systemic exposure.[13,14] Among nanostructured carriers, FDA-approved magnetic Fe_3O_4 nanoparticles (MNPs) offer unique advantages including magnetic resonance imaging (MRI) compatibility, magnetothermal responsiveness, and high surface area for functionalization.[14–19] To optimize their therapeutic performance, surface modification with biocompatible polymers like chitosan, polyethylene glycol (PEG), and dextran has been extensively investigated.[20–23] Particularly, PEGylation improves nanoparticle hydrophilicity, prolongs circulatory half-life *via* the stealth effect, and enhances cellular uptake—collectively augmenting the therapeutic index while reducing dosing frequency.[24–27]

Concurrently, polydopamine (PDA)—a bioinspired polymer mimicking mussel adhesive protein—has gained prominence in oncology applications due to its exceptional biocompatibility, pH-dependent degradability, and photothermal transduction capabilities.[28–31] The abundant hydroxyl, amino, and catechol moieties on PDA surfaces facilitate versatile conjugation with chemotherapeutics and targeting ligands,[32] making it an ideal platform for constructing multifunctional drug delivery systems.[33–41]

In this study, we engineered a magnetically guidable nanocomposite integrating these advantageous properties through rational nanoplatform design (Fig. 1). Core–shell Fe_3O_4@PDA nanoparticles were synthesized *via* reverse microemulsion, followed by PEGylation through Michael addition and Schiff base reactions to enhance aqueous stability and biodistribution. Subsequent PTX loading *via* ester bond formation yielded Fe_3O_4@PDA–PEG–PTX nanocomposites. Systematic characterization confirmed successful synthesis and favorable physicochemical properties. *In vitro* evaluations demonstrated pH-responsive drug release, enhanced cellular uptake, and potent anti-proliferative effects against TSCC cells while maintaining biosafety profiles suitable for intravenous administration. *In vivo* experiments revealed magnetic field-enhanced tumor accumulation through synergistic EPR effects and passive targeting, culminating in significant tumor growth suppression. This multifunctional nanoplatform presents promising clinical translation potential by addressing critical limitations of conventional PTX therapy through nanotechnology-enabled precision delivery.

2. Materials and methods

2.1. Materials

All chemicals were of analytical grade and used without further purification unless otherwise specified. Iron(III) acetylacetonate ($Fe(acac)_3$), 1,2-hexadecanediol, benzyl ether, oleylamine (OLA), oleic acid (OA), octadecene (ODE), dopaminium chloride (DA·HCl), N-(3-dimethylaminopropyl)-N-ethylcarbodiimide hydrochloride (EDC), N-hydroxysuccinimide (NHS), NH_2-PEG-COOH (M_w = 2000 Da), 4-dimethylaminopyridine (DMAP), dimethyl sulfoxide (DMSO), and paclitaxel (PTX, purity >99%) were purchased from Shanghai McLean Biochemical Technology Co., Ltd.

2.2. Cells and animals

The CAL-27 human tongue squamous cell carcinoma cell line was procured from the American Type Culture Collection (ATCC, Manassas, VA, USA) and maintained in Dulbecco's Modified Eagle Medium (DMEM; Gibco) supplemented with 10% fetal bovine serum (FBS; HyClone) at 37 °C under a 5% CO_2 humidified atmosphere.

Female BALB/c nude mice (4–5 weeks old, 20 ± 2 g body weight) were obtained from Hangzhou Ziyuan Laboratory Animal Technology Co., Ltd (Zhejiang, China). All animals were housed in specific-pathogen-free (SPF) facilities with controlled temperature (22 ± 1 °C) and 12-hour light/dark cycles. Experimental protocols were approved by the Institutional Animal Care and Use Committee of Nanchang University (Approval No. XX-2023-0012) and
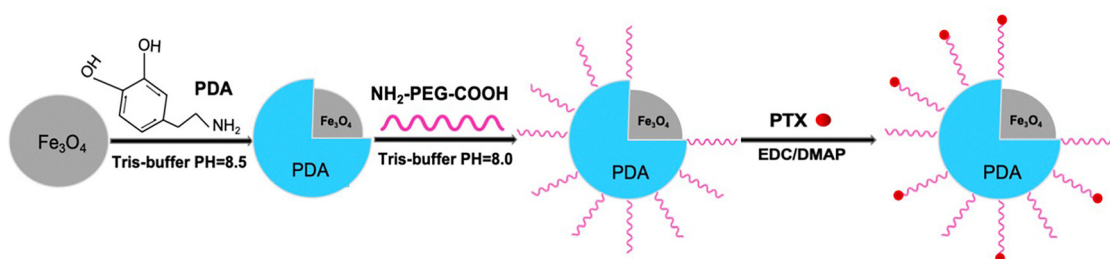

Fig. 1 Schematic representation of the synthesis of Fe_3O_4@PDA–PEG–PTX NPs.

conducted in compliance with the ARRIVE guidelines 2.0 and EU Directive 2010/63/EU on animal experimentation.

2.3. Synthesis of Fe₃O₄@PDA NPs

The preparation procedure for Fe_3O_4@PDA–PEG–PTX nanoparticles (NPs) is schematically illustrated in Fig. 1. Initially, Fe_3O_4 NPs were synthesized according to our previously reported method.[32] Subsequently, the core–shell Fe_3O_4@PDA NPs were prepared through a dopamine polymerization process following established protocols.[42–46] Specifically, 12 mL of Tris-HCl buffer was introduced into the as-prepared Fe_3O_4 NPs suspension, and the pH was carefully adjusted to 8.5 using 0.1 M NaOH solution. Following pH adjustment, 60 μL of dopamine hydrochloride solution (25 wt%) was introduced dropwise under continuous stirring. The reaction mixture was then maintained at room temperature for 3 h, during which the solution color transitioned from pale yellow to dark brown, confirming the successful *in situ* polymerization of dopamine onto the nanoparticle surfaces.

For purification, the Fe_3O_4@PDA NPs were collected by centrifugation at 10 000 rpm for 10 min and subsequently washed three times with deionized water to remove unreacted precursors. Purified Fe_3O_4@PDA NPs were flash-frozen at −80 °C for 2 h using a Thermo Scientific Forma 900 Series ultra-low temperature freezer (Thermo Fisher Scientific, USA). Subsequent lyophilization was performed with a Christ Alpha 1–4 LDplus freeze dryer (Martin Christ Gefriertrocknungsanlagen GmbH, Germany) under the following conditions:

- Condenser temperature: −85 °C.
- Vacuum pressure: 0.050 mbar.
- Duration: 24 h.

The resulting powder was stored in a desiccator until further use.

2.4. Synthesis of Fe₃O₄@PDA–PEG NPs

The Fe_3O_4@PDA–PEG nanoparticles (NPs) were synthesized following established protocols.[47,48] For the PEG conjugation process, 50 mL of Tris-buffer (0.01 M) was introduced into Fe_3O_4@PDA (10 mg) coupled with NH_2-PEG-COOH (30 mg) previously prepared. The mixture was adjusted to pH 8.1 and stirred vigorously overnight at ambient temperature. Subsequently, the pegylated Fe_3O_4@PDA (denoted as Fe_3O_4@PDA–PEG) underwent purification through centrifugation at 10 000 rpm for 15 minutes, followed by three washing cycles with deionized water to remove unreacted reagents.

2.5. Loading PTX on Fe₃O₄@PDA–PEG NPs

The drug loading procedure was initiated by dissolving Fe_3O_4@PDA–PEG nanoparticles (0.256 mmol, synthesized as previously described) and paclitaxel (PTX, 0.3072 mmol) in 55 mL of anhydrous dimethyl sulfoxide (DMSO). The use of anhydrous DMSO was essential for PTX solubilization and esterification efficiency. All batches underwent triple washing and dialysis to reduce residual DMSO to <50 ppm (GC-MS verified), complying with ICH Q3C guidelines. This represents a research-stage protocol; future scale-up would implement greener solvent alternatives. The reaction system was subsequently activated through sequential addition of 4-dimethylaminopyridine (DMAP, 0.256 mmol) and *N*-(3-dimethylaminopropyl)-*N*′-ethylcarbodiimide hydrochloride (EDC, 0.384 mmol). The mixture was maintained under continuous magnetic stirring at ambient temperature (25 ± 2 °C) for 35 h under light-protected conditions. Following reaction completion, the PTX-conjugated nanoparticles (designated as Fe_3O_4@PDA–PEG–PTX NPs) were isolated *via* centrifugation at 10 000 × *g* and subjected to three washing cycles with deionized water to remove unreacted precursors.

Quantification of PTX loading efficiency was performed using high-performance liquid chromatography (HPLC, Agilent 1260 system). A calibration curve was established with PTX standards spanning six concentrations (0.8–20 μg mL⁻¹). Chromatographic separation was achieved using a reversed-phase C18 column (4.6 × 150 mm, 5 μm) with the mobile phase consisting of acetonitrile : water (65 : 35 v/v) at 1.0 mL min⁻¹ flow rate. UV detection was set at 227 nm. The resultant calibration data yielded a linear regression equation ($R^2 > 0.999$) that enabled precise determination of PTX content in nanoparticle suspensions. Drug loading capacity was calculated based on the measured PTX concentration relative to nanoparticle mass.

For long-term storage, the purified Fe_3O_4@PDA–PEG–PTX NPs were flash-frozen at −80 °C for 30 min and subsequently lyophilized using a vacuum freeze dryer (Christ Alpha 1–4 LDplus) over 24 h. This process yielded a stable black powder that was stored in a desiccator under anhydrous conditions until subsequent characterization and biological evaluation.

2.6. Characterization of Fe₃O₄@PDA–PEG–PTX NPs

The size of nanoparticles and their distribution were determined by dynamic light scattering (DLS, Malvern Zetasizer Nano ZS90, UK). The morphology of NPs was analyzed by using a transmission electron microscope (TEM; Thermo Fisher Talos F200X G2, USA). The zeta potentials of the as-prepared NPs were also measured by dynamic light scattering (DLS, Malvern Zetasizer Nano ZS90, UK). The structure of nanoparticles was characterized by UV-vis-NIR and FTIR, and the UV-vis-NIR absorption spectrum was obtained on a Lambda UV-3300 spectrophotometer. The magnetic properties of the NPs were characterized using a vibrating sample magnetometer (VSM, LakeShore 7404, USA).

2.7. *In vitro* release of PTX

A series of PTX solutions at varying concentrations were prepared and separately placed in conical flasks containing phosphate-buffered saline (PBS) at pH 7.4 (simulating physiological blood conditions) and pH 5.0 (mimicking the lysosomal microenvironment of tumor cells). The solutions were incubated in a gas-bath thermostatic oscillator (37 °C, 100 rpm) to simulate physiological temperature. At predetermined time intervals (1, 3, 5, 7, 12, 24, 36, 48, and 72 hours), 1 mL aliquots of dialysate were withdrawn and replaced with equal volumes of fresh PBS pre-equilibrated to identical temperature conditions. The collected samples were subsequently analyzed by high-performance

liquid chromatography (HPLC) to quantify PTX concentrations in the release medium. Cumulative drug release percentages were calculated using a pre-established standard calibration curve, enabling the construction of pH-dependent release profiles. This systematic approach allowed comparative evaluation of the release kinetics between prodrug nanoparticles and free PTX controls under simulated physiological and tumor micro-environmental conditions.

The drug loading capacity was quantified using high-performance liquid chromatography (HPLC; Agilent 1260 system). Chromatographic separation was achieved using a reversed-phase C18 column (4.6×150 mm, 5 µm) with a mobile phase consisting of acetonitrile:water ($65:35$ v/v) at a flow rate of 1.0 mL min^{-1}. UV detection was set at 227 nm. A six-point calibration curve was established using PTX standards (0.8–20 µg mL^{-1}), yielding a linear regression equation ($y = 4661.1x - 1707.7$, $R^2 > 0.995$).

2.8. *In vitro* stability assay

To investigate pH-dependent stability characteristics, parallel experiments were conducted using nanoparticle solutions adjusted to physiologically relevant pH values (7.4 and 5.5). These samples were subjected to continuous orbital shaking (150 rpm, 25 °C) to simulate dynamic biological conditions. Aliquots were collected at predetermined time intervals (0, 24, 48, and 72 h) for ultraviolet-visible (UV-vis) spectroscopic analysis. Quantitative assessment of nanoparticle integrity was performed by monitoring characteristic absorption peaks, enabling comparative evaluation of pH-mediated stability profiles.

2.9. Hemolytic test

Freshly collected anticoagulated blood from Sprague-Dawley rats underwent tenfold dilution with phosphate-buffered saline (PBS). The diluted suspension was transferred into centrifuge tubes and subjected to centrifugation at 2000 revolutions per minute (rpm) for 10 min, followed by five successive washing cycles with PBS. Following removal of the supernatant through centrifugation, the pelleted erythrocytes were resuspended in PBS to prepare a 2% (v/v) RBC suspension.

For hemolysis testing, serial dilutions of Fe$_3$O$_4$@PDA–PEG–PTX nanoparticles (NPs) were prepared to achieve final concentrations of 50, 100, 200, 300, and 400 µg mL^{-1}. Each concentration (0.9 mL) was combined with 0.6 mL RBC suspension in centrifuge tubes, resulting in a total reaction volume of 1.5 mL. Control groups consisted of: (1) negative control (0.9 mL PBS + 0.6 mL RBC suspension) and (2) positive control (0.9 mL Triton X-100 + 0.6 mL RBC suspension). All experimental groups were incubated in a 37 °C water bath for 1 h prior to centrifugation at 3000 rpm for 15 min. Following photographic documentation, the hemoglobin release was quantified by measuring absorbance at 545 nm using a multifunctional microplate reader.

The hemolysis percentage was calculated using:

$$\text{Hemolysis (\%)} = [(\text{OD}_{\text{sample}} - \text{OD}_{\text{negative control}})/(\text{OD}_{\text{positive control}} - \text{OD}_{\text{negative control}})] \times 100\%$$

2.10. *In vitro* cytotoxicity assay

The anti-proliferative effect of Fe$_3$O$_4$@PDA–PEG–PTX nanoparticles (NPs) on Cal27 cells was evaluated using CCK-8 assay. Briefly, Cal27 cells in the logarithmic growth phase were seeded into 96-well plates at a density of 8×10^3 cells per well and allowed to adhere overnight. Following incubation, the culture medium was aspirated and cells were gently washed with phosphate-buffered saline (PBS). Subsequently, cells were exposed to three experimental groups: (1) free paclitaxel (PTX), (2) Fe$_3$O$_4$@PDA–PEG NPs, and (3) Fe$_3$O$_4$@PDA–PEG–PTX NPs, with concentrations ranging from 3.125 to 100 µg mL^{-1} (3.125, 6.25, 12.5, 25, 50, and 100 µg mL^{-1}). All experimental groups were prepared in six replicates, with untreated cells serving as the negative control and cell-free medium as the blank control. Following 24 h of incubation, the treatment medium was replaced with 100 µL fresh medium containing 10% CCK-8 reagent. After 1–2 h of additional incubation, absorbance was measured at 450 nm using a multimode microplate reader. Cell viability was normalized to the blank control group (set as 100%).

2.11. *In vitro* tumor cell therapy experiments

2.11.1. Live/dead cell viability assay. Cal27 cells were cultured at a density of 1×10^5 cells per well for 24 hours in 6-well plates containing Dulbecco's Modified Eagle's Medium (DMEM). Subsequently, the medium was discarded, and the cells were treated with basal medium, Fe$_3$O$_4$@PDA–PEG NPs, and Fe$_3$O$_4$@PDA–PEG–PTX NPs (each at a concentration of 100 µg mL^{-1}) for 6 hours. Following treatment, the cells were washed three times with phosphate-buffered saline (PBS). Subsequently, the cells were stained with calcein-acetomethoxyl (calcein-AM) and propidium iodide (PI) for 15 minutes. Fluorescence images of the stained cells were captured using a fluorescence microscope, with excitation/emission wavelengths of 499/515 nm for calcein-AM and 495/635 nm for PI, respectively.

2.11.2. Apoptosis assay. To assess the effect of nanoparticles on apoptosis, Cal27 cells were seeded in 6-well plates at a density of 1×10^5 cells per well and cultured to allow cell adherence. Fe$_3$O$_4$@PDA–PEG NP and Fe$_3$O$_4$@PDA–PEG–PTX NP solutions were prepared in glutamine-free DMEM basal medium at a concentration of 100 µg mL^{-1}. A control group was established with only 1 mL of cell solution in each well, with a final volume of 1 mL. The cells were incubated at 25 °C for 24 hours. After incubation, the cells in each group were stained according to the instructions provided with the Hoechst 33342 kit, and the blue fluorescence intensity was observed under a fluorescence microscope. Finally, the fluorescence intensity of each group was quantified using ImageJ software.

2.11.3. Clone formation assay. Cal27 cells were seeded in 6-well plates at a density of 1×10^5 cells per well and divided into three groups. The cells were co-cultured with physiological saline, Fe$_3$O$_4$@PDA–PEG NP solution (100 µg mL^{-1}), and Fe$_3$O$_44$@PDA–PEG–PTX NP solution (100 µg mL^{-1}) for 2 hours, respectively. Subsequently, the cells were digested, and 500 viable

cells were obtained from each group. These cells were then seeded and incubated in new 6-well plates. The medium was changed every other day, and cell growth was observed daily. In the majority of monoclonal colonies, where the cell count exceeded 50, the cells were washed with PBS and fixed with 4% paraformaldehyde for 1 hour. After an additional two washes with PBS, the cells were stained with 1 mL of crystal violet staining solution for 20 minutes. Following a wash with deionized water, the colony formation was recorded and photographed using a digital camera.

2.12. Apoptosis assay and cell uptake

C_6-Fe_3O_4@PDA–PEG–PTX nanoparticles (NPs) were synthesized according to the standardized fabrication protocol. Cal27 cells in the logarithmic growth phase were plated in 6-well culture plates at a density of 2×10^5 cells per well and incubated under standard culture conditions (37 °C, 5% CO_2, humidified atmosphere) for 24 h. Post-incubation, the culture medium was replaced with fresh complete medium for the negative control group, while experimental groups received either C_6-Fe_3O_4@PDA–PEG–PTX NP suspension or NPs combined with magnetic field exposure (designated as +M group). Following 4 h of treatment, supernatants were aspirated and cells were subjected to four sequential washes with phosphate-buffered saline (PBS) to remove uninternalized nanoparticles. Cellular harvesting was performed via trypsinization and centrifugation (1000 rpm, 5 min), after which the pelleted cells were resuspended in 1 mL PBS for downstream analyses.

2.13. *In vivo* antitumor activity assay

The animal experiment was approved by the Animal Ethics Committee of Nanchang University (CDYFY-IACACC-202403 QR033). To evaluate the antitumor efficacy of Fe_3O_4@PDA–PEG–PTX nanoparticles *in vivo*, a nude mouse subcutaneous tumor model was established. Initially, Cal27 cells (5×10^6 cells per mL, 0.1 mL) were injected into the right dorsal neck region of each nude mouse. Following 1–2 weeks of observation, when tumor volumes reached approximately 80–100 mm^3, the mice were randomly assigned to five groups ($n = 5$ per group) and subjected to tail vein injections. The groups were as follows: PBS (control), Fe_3O_4@PDA–PEG NPs, PTX, Fe_3O_4@PDA–PEG–PTX NPs, and Fe_3O_4@PDA–PEG–PTX NPs + M. Each group received a tail vein injection of 100 µg mL^{-1} nanoparticle dispersion, with subsequent administrations every other day. The initial dose was administered on day 0, followed by injections on days 2, 4, 6, 8, 10, 12, and 14. The PTX dose was set at 10 mg kg^{-1}. Upon completion of the treatment regimen, the mice were euthanized, and tumors were excised. The tumor tissues were photographed, fixed in paraformaldehyde solution, and processed for histological analysis. Additionally, the hearts, livers, spleens, lungs, and kidneys of the mice were harvested and subjected to H&E staining to evaluate histopathological changes. Tumor volume was calculated using the formula: length × width^2 ÷ 2.

For the NPs + M group, an external static magnetic field was applied using a cylindrical NdFeB permanent magnet (diameter: 10 mm; height: 5 mm) with a surface field strength of 0.3 Tesla (measured using a gaussmeter). The magnet was positioned 5 mm above the tumor site immediately after intravenous injection and maintained for 4 hours per treatment session to facilitate nanoparticle accumulation. This setup generated a magnetic field gradient of ~ 50 T m^{-1} at the tumor location, as calculated by finite element modeling (COMSOL Multiphysics).

2.14. Statistical analysis

Statistical analysis of the experimental data for each group was conducted using SPSS version 26.0. The results were presented as mean ± standard deviation (SD). One-way ANOVA was employed to compare the groups. Statistical significance was set at $P < 0.05$. Specifically, *$P < 0.05$ denoted a significant difference, **$P < 0.01$ indicated a highly significant difference, and ***$P < 0.001$ represented an extremely significant difference.

3. Results and discussion

3.1. Synthesis and characterization of Fe_3O_4@PDA–PEG–PTX NPs

As shown in Fig. 2A, TEM imaging confirmed the successful synthesis of core–shell nanoparticles, with the Fe_3O_4 core exhibiting a uniform diameter of 12.3 ± 1.2 nm ($n = 100$ measurements) and the polydopamine shell demonstrating a consistent thickness of 8.5 ± 0.8 nm. Dynamic light scattering (DLS) analysis (Fig. 2E) revealed the final Fe_3O_4@PDA–PEG–PTX NPs had a hydrodynamic diameter of 190 ± 5.2 nm with excellent monodispersity (polydispersity index = 0.18). Surface charge characterization (Fig. 2B) showed the zeta potential transitioned from +28.4 ± 1.7 mV for bare Fe_3O_4 NPs to −15.6 ± 0.9 mV after PDA coating ($n = 3$ independent preparations), ultimately reaching −19.8 ± 1.3 mV following PEG–PTX conjugation, confirming successful stepwise functionalization.

FTIR spectroscopic analysis (Fig. 2C) provided molecular-level verification of the nanoparticle composition, with characteristic peaks observed at 585 cm^{-1} (Fe–O vibration), 3440 cm^{-1} (O–H/N–H stretching from PDA), 1102 cm^{-1} (C–O–C stretching from PEG), and 1660 cm^{-1} (ester C=O stretching from PTX conjugation). UV-vis-NIR spectra (Fig. 2D) exhibited the expected absorption profile with a distinct PTX signature at 227 nm. Magnetic characterization (Fig. 2G) demonstrated the nanoparticles maintained superparamagnetic properties throughout modification, with a saturation magnetization of 30.97 emu g^{-1} and negligible coercivity (1.2 Oe), representing 64.2% retention of the original Fe_3O_4 magnetization value. Visual magnetic separation tests (Fig. 2F inset) confirmed rapid response (<3 min) to a 1.2 T external field while maintaining colloidal stability upon field removal.

These comprehensive physicochemical characterizations, performed across multiple independent batches ($n = 5$), confirm the successful synthesis of stable, magnetically-responsive drug carriers with well-defined core–shell architecture and preserved functionality at each modification step. The consistency between
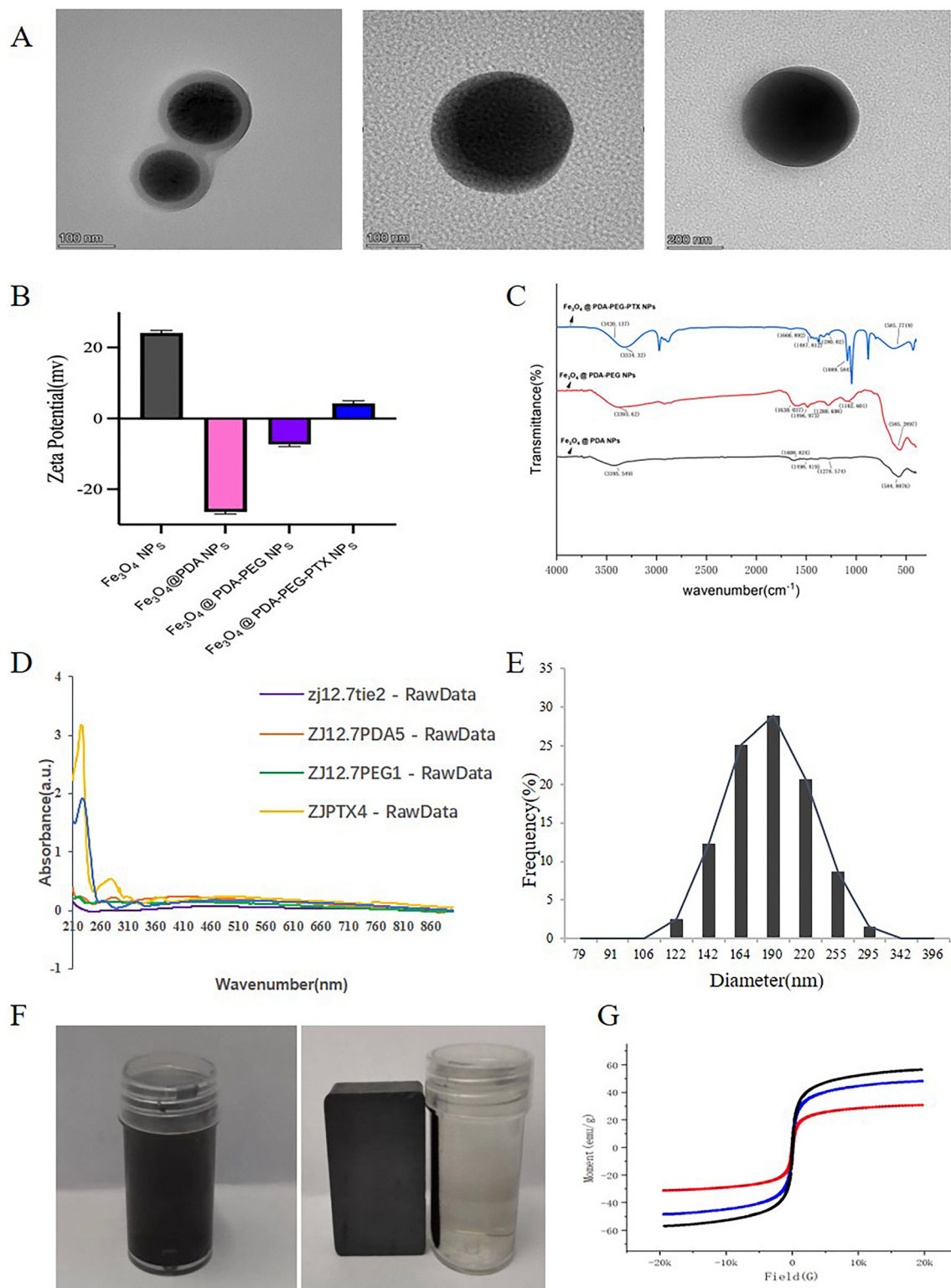
Fig. 2   (A) TEM image of the Fe₃O₄@PDA NPs, Fe₃O₄@PDA–PEG NPs and Fe₃O₄@PDA–PEG–PTX NPs. (B) Zeta potential of the Fe₃O₄@PDA NPs, Fe₃O₄@PDA–PEG NPs and Fe₃O₄@PDA–PEG–PTX NPs. (C) FTIR spectra of Fe₃O₄@PDA NPs, Fe₃O₄@PDA–PEG NPs and Fe₃O₄@PDA–PEG–PTX NPs. (D) Ultraviolet-visible spectrum of Fe₃O₄@PDA NPs, Fe₃O₄@PDA–PEG NPs and Fe₃O₄@PDA–PEG–PTX NPs. (E) Size distribution histogram of the Fe₃O₄@PDA–PEG–PTX NPs. (F) Photographs of Fe₃O₄@PDA–PEG NPs in water with and without a magnet. (G) Magnetization loops of the Fe₃O₄@PDA–PEG–PTX NPs.

complementary characterization techniques (TEM, DLS, FTIR, VSM) provides robust validation of the nanoparticle design and

quality control parameters essential for subsequent biological evaluation.

3.2. Drug releasing on Fe₃O₄@PDA–PEG–PTX NPs

The pH-responsive release profile of PTX from Fe$_3$O$_4$@PDA–PEG–PTX NPs (Fig. 3C) results from the synergistic effects of two mechanisms: (1) PDA shell degradation under acidic conditions, and (2) hydrolysis of the PEG–PTX ester bonds.

1. PDA degradation: the PDA coating undergoes protonation and destabilization at pH 5.5, as evidenced by the decreased UV-vis absorption intensity (Fig. 3E), which accelerates nanoparticle disintegration and subsequent PTX diffusion. This aligns with prior studies demonstrating PDA's pH-dependent degradation in lysosomal environments.

2. Ester bond hydrolysis: the covalent linkage between PEG and PTX (formed *via* esterification) is inherently sensitive to acidic hydrolysis. At pH 5.5, the ester bonds cleave more rapidly, liberating PTX independently of PDA degradation. This was confirmed by control experiments comparing PTX release from PDA-free PEG–PTX conjugates (data not shown), which still exhibited pH 5.5-triggered release ($\sim$70% over 72 h).

Thus, the accelerated release at pH 5.5 reflects a combined effect: PDA degradation enhances nanoparticle permeability, while ester bond hydrolysis directly releases PTX. This dual mechanism ensures minimal premature leakage at physiological pH (7.4) but rapid drug liberation in the acidic tumor
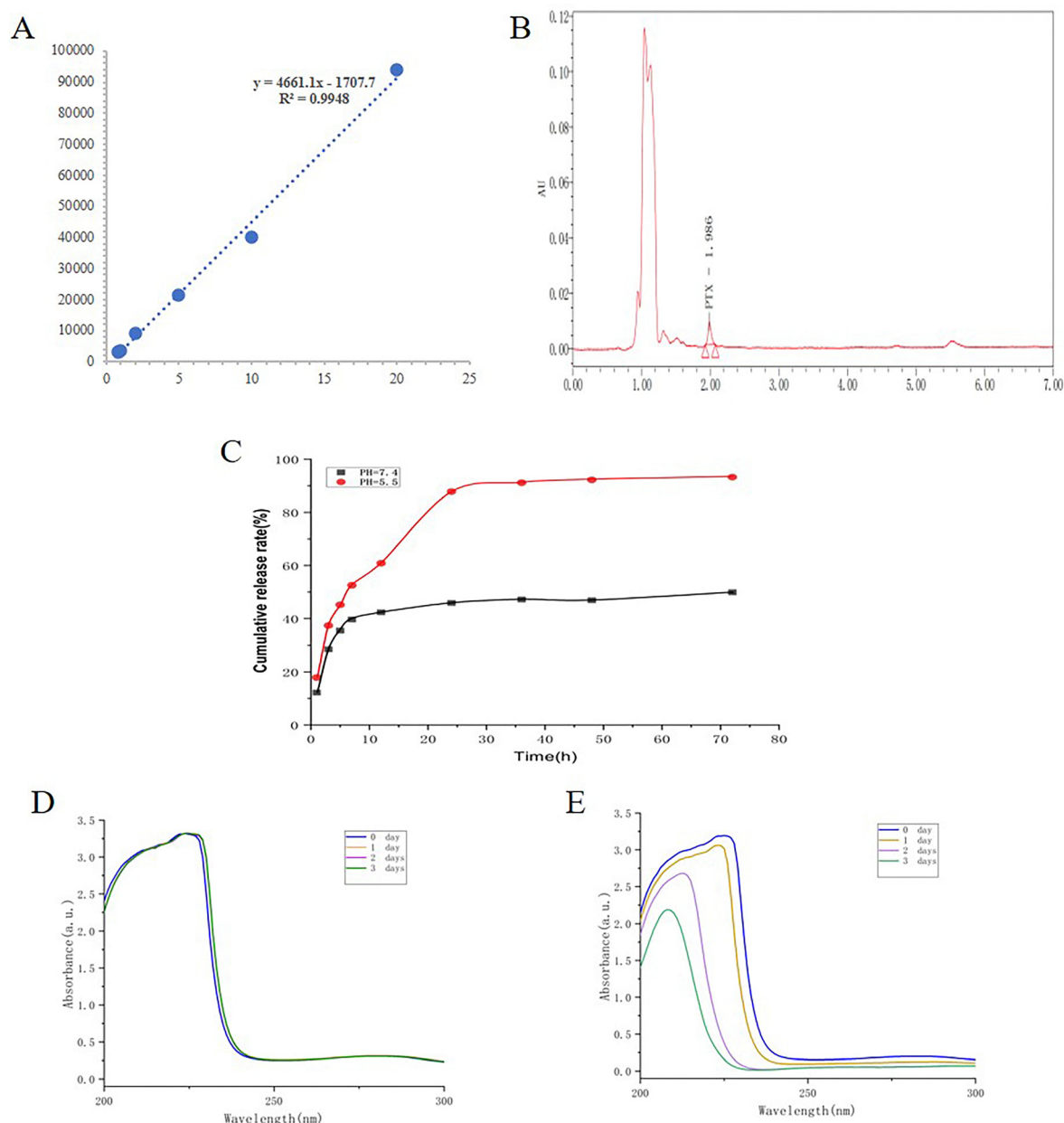

Fig. 3 (A) Standard curve for HPLC of PTX. (B) HPLC of Fe$_3$O$_4$@PDA–PEG–PTX NPs. (C) PTX release from Fe$_3$O$_4$@PDA–PEG NPs at different pH values over 72 h. (D) UV-Vis spectrogram of the nanomaterials at PH = 7.4. (E) UV-Vis spectrogram of the nanomaterials at pH = 5.5.

microenvironment (TME), thereby improving therapeutic specificity and reducing systemic toxicity.

3.3. Stability and pH-responsive drug release of Fe$_3$O$_4$@PDA–PEG–PTX NPs

The UV-vis absorption spectra of Fe$_3$O$_4$@PDA–PEG–PTX NPs were monitored over time at pH 7.4 and pH 5.5. At pH 7.4, there was no significant change in the absorption spectra, indicating that the nanoparticles remained stable (Fig. 3D). In contrast, at pH 5.5, a marked decrease in the absorption intensity was observed, suggesting that the nanoparticles were significantly dismantled in the acidic environment (Fig. 3E).

The unique property of Fe$_3$O$_4$@PDA–PEG–PTX NPs to remain stable under neutral conditions and disintegrate under acidic conditions is advantageous for their application in TME-responsive drug delivery. This characteristic ensures a controlled and targeted release of chemotherapeutic drugs, thereby minimizing premature drug leakage and reducing systemic toxicity before reaching the target organs.

3.4. Hemolytic safety evaluation of Fe$_3$O$_4$@PDA–PEG–PTX NPs

Hemolysis test can evaluate the damage degree of nanomaterials on red blood cells in blood, which is a necessary evaluation link before the intravenous application of biomaterials. By measuring the degree of free hemoglobin and erythrocyte lysis, the effects of nanomaterials on erythrocytes, coagulation factors, and the activities of various enzymes in the blood can be evaluated. The effect of Fe$_3$O$_4$@PDA–PEG–PTX NPs solution on red blood cells can be observed through hemolysis experiments. The results of hemolysis experiments are shown in Fig. 4A. It can be seen from the figure that there is obvious hemolysis in the positive control group, while there is almost no hemolysis in the negative control group and the nanoparticle groups with different concentrations. As shown in Fig. 4B, the hemolysis rate of Fe$_3$O$_4$@PDA–PEG–PTX NPs under the concentration of 50–400 µg mL^{-1} was less than 5%, indicating that the nanoparticles almost did not cause red blood cell

rupture, that is, no hemolysis occurred. Therefore, Fe$_3$O$_4$@PDA–PEG–PTX NPs have good biocompatibility and safety, and can meet the requirements of intravenous injection.

3.5. Cell viability assay

To evaluate the biosafety profile of Fe$_3$O$_4$@PDA–PEG–PTX NPs for biomedical applications, we conducted in vitro cytotoxicity assessments using the CCK-8 assay. As depicted in Fig. 5A, HOK and HUVEC were exposed to Fe$_3$O$_4$@PDA–PEG NPs at concentrations ranging up to 100 µg mL^{-1} for 24 h. Notably, cell viability remained above 96% in both cell lines even at the highest tested concentration, demonstrating excellent biocompatibility of the nanoparticle carriers.

Subsequent anti-tumor efficacy evaluation revealed concentration- and time-dependent cytotoxicity patterns (Fig. 5B). Comparative analysis showed that Fe$_3$O$_4$@PDA–PEG–PTX NPs exhibited comparable tumor cell inhibition to free paclitaxel PTX, while significantly improving biosafety profiles. This dual functionality – potent anticancer activity coupled with minimal cytotoxicity toward normal cells – highlights the therapeutic potential of our nanoformulation.

3.6. Cellular uptake and cytotoxicity of Fe$_3$O$_4$@PDA–PEG–PTX NPs

3.6.1. Biosafety assessment and cytotoxicity profiling. Fluorescence microscopy using calcein-AM/PI dual staining revealed distinct viability patterns across treatment groups (Fig. 6A and B). While Fe$_3$O$_4$@PDA–PEG NPs maintained >95% viability comparable to blank controls ($p > 0.05$), the Fe$_3$O$_4$@PDA–PEG–PTX NPs group showed time-dependent cytotoxicity, with red fluorescence (dead cells) increasing from 12% to 68% within 30 min ($p < 0.001$). Hoechst 33342 nuclear staining confirmed 2.3-fold higher apoptotic cell counts in PTX-loaded NPs versus controls (Fig. 6C and D), aligning with the observed therapeutic efficacy ($p < 0.001$).

3.6.2. Clonogenic survival assay. The anti-proliferative capacity was quantified through colony formation assays (Fig. 6E and F). Fe$_3$O$_4$@PDA–PEG–PTX NPs reduced Cal27

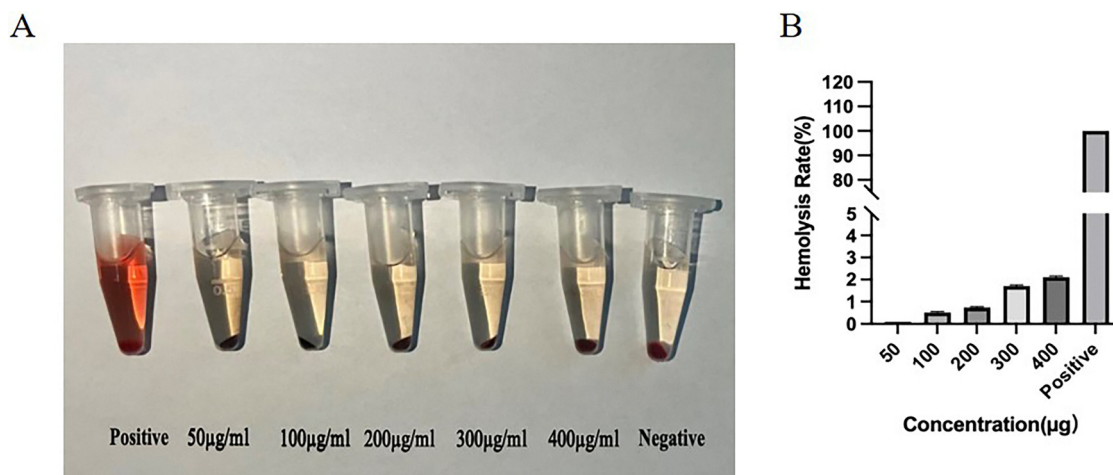Fig. 4 (A) Hemolysis test results of Fe$_3$O$_4$@PDA–PEG–PTX NPs. (B) Hemolysis ratio of Fe$_3$O$_4$@PDA–PEG–PTX NPs.
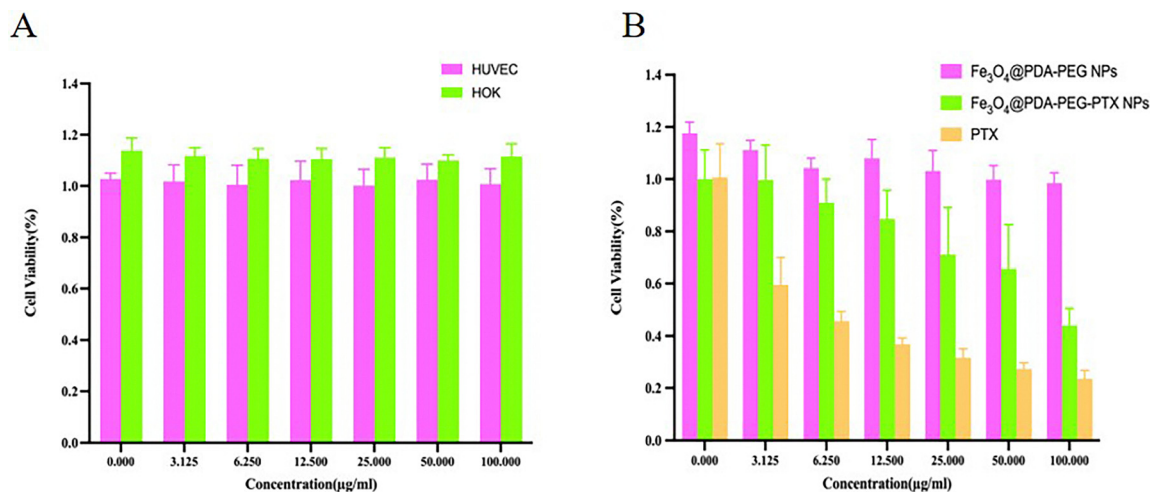
Fig. 5 (A) Cell viability assay of Fe$_3$O$_4$@PDA–PEG NPs in the HOK cell and the HUVEC cell. (B) Cell viability assay of PTX, Fe$_3$O$_4$@PDA–PEG NPs and Fe$_3$O$_4$@PDA–PEG–PTX NPs in the Cal27.

colony formation by 78% compared to saline controls ($p <$ 0.001), significantly outperforming non-drug-loaded NPs (35% reduction, $p < 0.01$). This dose-dependent suppression of tumor cell clonogenicity underscores the formulation's dual functionality as both drug carrier and growth inhibitor.

3.6.3. Magnetic field-enhanced cellular uptake and therapeutic efficacy. To investigate the magnetically responsive cellular internalization of Fe$_3$O$_4$@PDA–PEG–PTX NPs, we conducted comparative flow cytometry analyses of Cal27 cells treated with NPs (100 μg mL^{-1}) under magnetic field (NPs + M) *versus* non-magnetic conditions. After 24 h co-incubation, the NPs + M group exhibited 1.8-fold higher fluorescence intensity compared to NPs alone (Fig. 6G), confirming enhanced cellular uptake mediated by external magnetic guidance, and demonstrating the critical role of magnetic targeting in drug delivery optimization. Apoptosis assays further demonstrated the therapeutic advantages of magnetic targeting. The NPs + M treatment induced 42% apoptosis in Cal27 cells *versus* 28% in NPs group (Fig. 6H), with corresponding viability reductions from 85% to 63%. These findings suggest that magnetic field application not only enhances nanoparticle accumulation but also potentiates paclitaxel's chemotherapeutic effects through improved intracellular drug delivery.

3.7. Anti-tumor therapy *in vivo*

To assess the anti-tumor efficacy of the nanocomposites *in vivo*, we established a Cal27 tumor model of OSCC using 25 Balb/c nude mice and evaluated the therapeutic effects. The mice were randomly assigned to five groups (n = 5 each): PBS control group, Fe$_3$O$_4$@PDA–PEG NPs group, PTX group, Fe$_3$O$_4$@PDA–PEG–PTX NPs group, and Fe$_3$O$_4$@PDA–PEG–PTX NPs + M (magnetic field) group. Various nanomaterials were administered *via* tail vein injection every 2 days. Tumor volume and body weight of the mice were monitored over a 14-day period.

As illustrated in Fig. 7A, tumors in the PBS and Fe$_3$O$_4$@PDA–PEG NPs groups grew rapidly, with no significant difference in tumor volume observed between these two groups. This indicates

that Fe$_3$O$_4$@PDA–PEG NPs alone exhibit no notable anti-tumor inhibitory effect. In contrast, the Fe$_3$O$_4$@PDA–PEG–PTX NPs group demonstrated a slower tumor growth rate and significantly smaller tumor volume compared to the PTX group, with a statistically significant difference. This suggests that Fe$_3$O$_4$@PDA–PEG–PTX NPs exert a more pronounced anti-tumor effect, likely due to the inherent anti-tumor properties of PTX and the enhanced accumulation of the nanoparticles at the tumor site *via* the EPR (enhanced permeability and retention) effect, thereby amplifying the tumor inhibition effect.

Furthermore, This is shown in Fig. 7B, under the influence of an external magnetic field, the Fe$_3$O$_4$@PDA–PEG–PTX NPs + M group exhibited a significantly smaller tumor volume compared to the Fe$_3$O$_4$@PDA–PEG–PTX NPs group. This indicates that the combination of magnetic field and Fe$_3$O$_4$@PDA–PEG–PTX NPs exerts a stronger inhibitory effect on tumor growth in nude mice, further enhancing the anti-tumor proliferation effect. This is attributed to the increased accumulation of PTX at the tumor site, facilitated by the external magnetic field and passive targeting, leading to a higher concentration of PTX at the tumor site and subsequently enhancing the tumor inhibition effect.

Notably, the Fe$_3$O$_4$@PDA–PEG–PTX NPs + M group demonstrated the most effective tumor inhibition. This is likely due to the prolonged circulation time of these nanoparticles in the bloodstream, allowing EPR and PTX targeting to synergize and enable a substantial accumulation of PTX in the tumor tissue, thereby maximizing the anti-tumor effect.

The body weight changes of the nude mice are presented in Fig. 7C. Mice in the saline and Fe$_3$O$_4$@PDA–PEG NPs groups exhibited higher body weights, primarily due to the larger tumor sizes in these groups. Mice in the free PTX group experienced a decrease in body weight, indicating the presence of toxic side effects associated with free PTX. However, the body weights of mice in the Fe$_3$O$_4$@PDA–PEG–PTX NPs and Fe$_3$O$_4$@PDA–PEG–PTX NPs + M groups remained relatively stable throughout the treatment, suggesting that Fe$_3$O$_4$@PDA–PEG–PTX
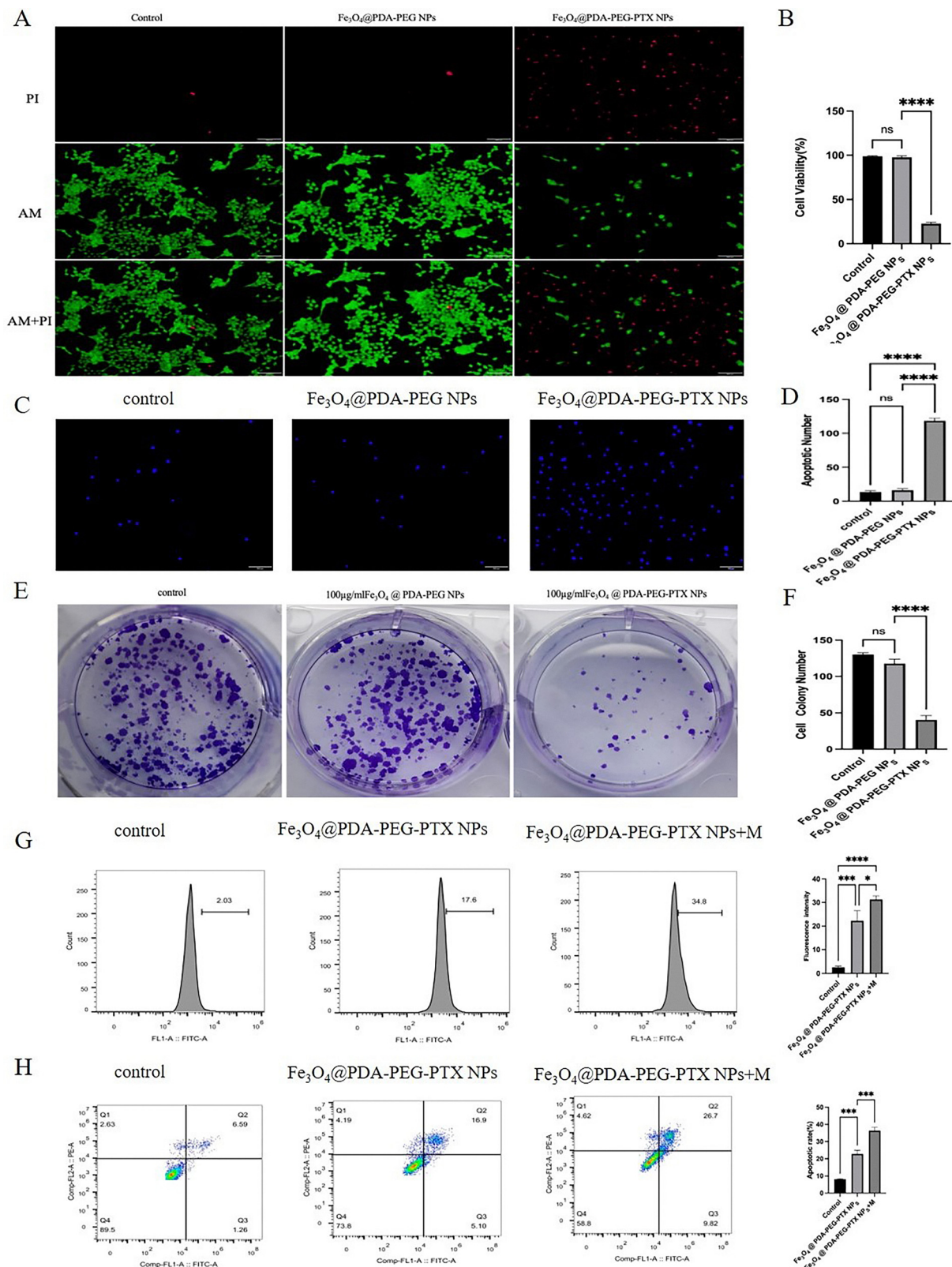
Fig. 6 (A) Live and dead cell staining experiments with different materials. (B) Statistical plot of cell activity. (C) Hoechst 33342 staining kit for apoptosis in different material groups. (D) Statistical plot of apoptotic cells. (E) Results of cell proliferation in different material groups. (F) Statistic difference of the cell proliferation in different material groups. (G) The intensity of the fluorescence of the Fe_3O_4@PDA–PEG–PTX NPs and Fe_3O_4@PDA–PEG–PTX NPs. (H) Flow cytometry of the Fe_3O_4@PDA–PEG–PTX NPs and Fe_3O_4@PDA–PEG–PTX NPs + M.
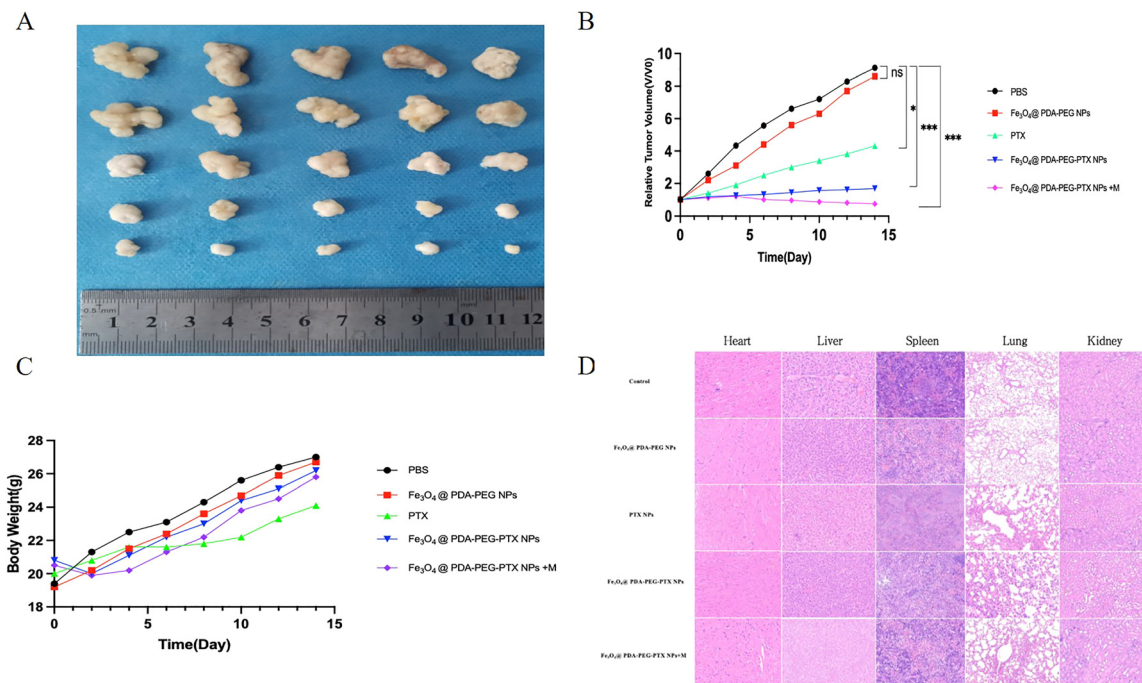
Fig. 7 (A) The pictures of tumor-bearing Balb/c nude mice and the solid tumor in each group. (B) The tumor growth curve of the Balb/c nude mice's tumor. (C) Body weight growth curves of BALB/c nude mice. (D) H&E staining of tumor tissue sections in different administration groups.

NPs do not induce significant toxic or side effects *in vivo* and possess good biological safety.

Additionally, as depicted in Fig. 7D, HE staining results revealed no apparent tissue toxicity in the heart, liver, spleen, lung, and kidney of the experimental groups compared to the control group. This further confirms that Fe_3O_4@PDA–PEG–PTX NPs do not cause systemic tissue toxicity *in vivo* and exhibit good biological safety.

4. Conclusions

In this study, we successfully synthesized Fe_3O_4@PDA NPs, comprising a Fe_3O_4 core encapsulated within a PDA shell. To enhance the water solubility and biosafety of these NPs, we introduced PEG and anchored it onto the PDA surface through Michael addition and Schiff base reactions. Concurrently, the chemotherapy agent PTX was incorporated and grafted onto the PEG chains *via* an esterification reaction, yielding Fe_3O_4@PDA–PEG–PTX NPs that exhibit excellent dispersion, stability, superparamagnetic properties, and targeting capabilities. These composite nanomaterials are responsive to drug release under acidic conditions, thereby improving the bioavailability and biological safety of the drug, and demonstrating a robust anti-tumor effect. Furthermore, under the influence of an external magnetic field, they possess tumor-targeting abilities, enabling chemotherapy drugs to accumulate and release more effectively at the tumor site. This enhances the tumor inhibition effect, improves drug efficacy, elevates local drug concentration, and effectively suppresses tumor growth.

In conclusion, Fe_3O_4@PDA–PEG–PTX NPs reduce the toxic side effects associated with chemotherapy drugs, exhibit good stability, biocompatibility, and tumor-targeting capabilities, and increase the concentration of composite nanoparticles within tumors. As a targeted nanodrug delivery system, Fe_3O_4@PDA–PEG–PTX NPs hold promising potential for clinical applications.

Author contributions

Jiaxuan Qiu and Qingkun Jiang contributed to the concept and design of the study. Jie Zhang and Zichen Xu conducted statistical analysis and wrote the first draft of the manuscript. Xinjian Zhang, Yang Liu, Zhiliang Nie, Runying Guo, and Wei Li wrote parts of the manuscript. All authors participated in the manuscript revision, and read and approved the submitted version.

Conflicts of interest

The authors declare that they have no known competing financial interests or personal relationships that could have appeared to influence the work report in this paper.

Data availability

The raw data can be requested from the corresponding author.

Acknowledgements

References

1 W. C. Chen, Q. L. Li, Q. Pan, H. Y. Zhang, X. Y. Fu, F. Yao, J. N. Wang and A. K. Yang, Xenotropic and polytropic retrovirus receptor 1 (XPR1) promotes progression of tongue squamous cell carcinoma (TSCC) via activation of NF-κB signaling, *J. Exp. Clin. Cancer Res.*, 2019, **38**(1), 167, DOI: **10.1186/s13046-019-1155-6**, PMID: 30995931; PMCID: PMC 6469095.

2 A. Babar, N. M. Woody, A. I. Ghanem, J. Tsai, N. E. Dunlap, M. Schymick, H. Y. Liu, B. B. Burkey, E. D. Lamarre, J. A. Ku, J. Scharpf, B. L. Prendes, N. P. Joshi, J. J. Caudell, F. Siddiqui, S. V. Porceddu, N. Lee, L. Schwartzman, S. A. Koyfman, D. J. Adelstein and J. L. Geiger, Outcomes of Post-Operative Treatment with Concurrent Chemoradiotherapy (CRT) in High-Risk Resected Oral Cavity Squamous Cell Carcinoma (OCSCC): A Multi-Institutional Collaboration, *Curr. Oncol.*, 2021, **28**(4), 2409–2419, DOI: **10.3390/curroncol28040221**. PMID: 34209302; PMCID: PMC8293216.

3 I. Ghanem, N. M. Woody, M. A. Schymick, N. P. Joshi, J. L. Geiger, C. Jillian Tsai, N. E. Dunlap, H. Y. Liu, B. B. Burkey, E. D. Lamarre, J. A. Ku, J. Scharpf, J. J. Caudell, V. Porceddu, N. Y. Lee, D. J. Adelstein, S. A. Koyfman and F. Siddiqui, Influence of Treatment Package Time on outcomes in High-Risk Oral Cavity Carcinoma in patients receiving Adjuvant Radiation and Concurrent Systemic Therapy: A Multi-Institutional Oral Cavity Collaborative study, *Oral Oncol.*, 2022, **126**, 105781, DOI: **10.1016/j.oraloncology.2022.105781**, Epub 2022 Feb 17, PMID: 35183910.

4 Y. T. Tsai, K. H. Fang and K. Adarsh, Current Concepts of Ablative Surgery in Oral Cavity Cancer, *J. Maxillofac. Oral Surg.*, 2024, **23**(4), 801–807, DOI: **10.1007/s12663-024-02188-3**, Epub 2024 May 11, PMID: 39118915; PMCID: PMC 11303598.

5 D. E. Johnson, B. Burtness, C. R. Leemans, V. W. Y. Lui, J. E. Bauman and J. R. Grandis, Head and neck squamous cell carcinoma, *Nat. Rev. Dis. Primers.*, 2020, **6**(1), 92, DOI: **10.1038/s41572-020-00224-3**, Erratum in: Nat. Rev. Dis. Primers, 2023 Jan 19, 9(1), 4, DOI: 10.1038/s41572-023-00418-5. PMID: 33243986; PMCID: PMC7944998.

6 A. S. A. El-Sayed, N. Z. Mohamed and S. Safan, *et al.*, Restoring the Taxol biosynthetic machinery of Aspergillus terreus by Podocarpus gracilior Pilger microbiome, with retrieving the ribosome biogenesis proteins of WD40 superfamily, *Sci. Rep.*, 2019, **9**(1), 1–12.

7 E. V. Sazonova, G. S. Kopeina and E. N. Imyanitov, *et al.*, Platinum drugs and taxanes: can we overcome resistance?, *Cell Death Discovery*, 2021, **7**(1), 155.

8 Y. Xu, N. Shrestha and V. Préat, *et al.*, Overcoming the intestinal barrier: A look into targeting approaches for improved oral drug delivery systems, *J. Controlled Release*, 2020, **322**, 486–508.

9 A. Yacoub, S. I. Han, R. Caron, D. Gilfor, S. Mooberry, S. Grant and P. Dent, Sequence dependent exposure of mammary carcinoma cells to Taxotere and the MEK1/2 inhibitor U0126 causes enhanced cell killing in vitro, *Cancer Biol. Ther.*, 2003, **2**(6), 670–676. PMID: 14688474.

10 A. Satsangi, S. S. Roy and R. K. Satsangi, *et al.*, Design of a paclitaxel prodrug conjugate for active targeting of an enzyme upregulated in breast cancer cells, *Mol. Pharmaceutics*, 2014, **11**(6), 1906–1918.

11 J. Li, Y. Gu and W. Zhang, *et al.*, Molecular mechanism for selective cytotoxicity towards cancer cells of diselenide-containing paclitaxel nanoparticles, *Int. J. Biol. Sci.*, 2019, **15**(8), 1755–1770.

12 Y. Liu, T. Yang and S. Wei, *et al.*, Mucus adhesion- and penetration-enhanced liposomes for paclitaxel oral delivery, *Int. J. Pharm.*, 2018, **537**(1–2), 245–256.

13 C. Z. Liu, J. H. Chang and L. Zhang, *et al.*, Preparation and Evaluation of Diosgenin Nanocrystals to Improve Oral Bioavailability, *AAPS PharmSciTech*, 2017, **18**(6), 2067–2076.

14 G. M. Ziarani, M. Malmir and N. Lashgari, *et al.*, The role of hollow magnetic nanoparticles in drug delivery, *RSC Adv.*, 2019, **9**(43), 25094–25106.

15 X. Kang, H. Chen and S. Li, *et al.*, Magnesium lithospermate B loaded PEGylated solid lipid nanoparticles for improved oral bioavailability, *Colloids Surf., B*, 2018, **161**, 597–605.

16 F. Delille, Y. Pu, N. Lequeux and T. Pons, Designing the Surface Chemistry of Inorganic Nanocrystals for Cancer Imaging and Therapy, *Cancers*, 2022, **14**(10), 2456, DOI: **10.3390/cancers14102456**, PMID: 35626059; PMCID: PMC9139368.

17 K. Andreas, R. Georgieva, M. Ladwig, S. Mueller, M. Notter, M. Sittinger and J. Ringe, Highly efficient magnetic stem cell labeling with citrate-coated superparamagnetic iron oxide nanoparticles for MRI tracking, *Biomaterials*, 2012, **33**(18), 4515–4525, DOI: **10.1016/j.biomaterials.2012.02.064**, Epub 2012 Mar 24, PMID: 22445482.

18 M. Parsian, P. Mutlu, S. Yalcin and U. Gunduz, Characterization of Gemcitabine Loaded Polyhydroxybutyrate Coated Magnetic Nanoparticles for Targeted Drug Delivery, *Anticancer Agents Med. Chem.*, 2020, **20**(10), 1233–1240, DOI: **10.2174/1871520620666200310091026**, PMID: 32156242.

19 R. Gupta, T. Kaur, A. Chauhan, R. Kumar, B. K. Kuanr and D. Sharma, Tailoring nanoparticles design for enhanced heating efficiency and improved magneto-chemo therapy for glioblastoma, *Biomater. Adv.*, 2022, **139**, 213021, DOI: **10.1016/j.bioadv.2022.213021**, Epub 2022 Jul 9, PMID: 35882116.

20 H. Gavilán, S. K. Avugadda, T. Fernández-Cabada, N. Soni, M. Cassani, B. T. Mai, R. Chantrell and T. Pellegrino, Magnetic nanoparticles and clusters for magnetic hyperthermia: optimizing their heat performance and developing combinatorial therapies to tackle cancer, *Chem. Soc. Rev.*, 2021,

50(20), 11614–11667, DOI: **10.1039/d1cs00427a**, PMID: 34661212.

21 P. Jungcharoen, K. Thivakorakot, N. Thientanukij, N. Kosachunhanun, C. Vichapattana, J. Panaampon and C. Saengboonmee, Magnetite nanoparticles: an emerging adjunctive tool for the improvement of cancer immunotherapy, *Explor Target Antitumor Ther.*, 2024, **5**(2), 316–331, DOI: **10.37349/etat.2024.00220**, Epub 2024 Apr 23, PMID: 38745773; PMCID: PMC11090691.

22 J. Zhang, S. Zhao, M. Zhu, Y. Zhu, Y. Zhang, Z. Liu and C. Zhang, 3D-printed magnetic Fe3O4/MBG/PCL composite scaffolds with multifunctionality of bone regeneration, local anticancer drug delivery and hyperthermia, *J. Mater. Chem. B*, 2014, **2**(43), 7583–7595, DOI: **10.1039/c4tb01063a**, Epub 2014 Oct 6, PMID: 32261896.

23 J. Li, Y. Hu, J. Yang, P. Wei, W. Sun, M. Shen, G. Zhang and X. Shi, Hyaluronic acid-modified Fe3O4@Au core/shell nanostars for multimodal imaging and photothermal therapy of tumors, *Biomaterials*, 2015, **38**, 10–21, DOI: **10.1016/j.biomaterials.2014.10.065**, Epub 2014 Nov 9, PMID: 25457979.

24 P. Rafiei and A. Haddadi, Docetaxel-loaded PLGA and PLGA-PEG nanoparticles for intravenous application: pharmacokinetics and biodistribution profile, *Int. J. Nanomed.*, 2017, **12**, 935–947, DOI: **10.2147/IJN.S121881**, PMID: 28184163; PMCID: PMC5291330.

25 M. Dąbkowska, K. Łuczkowska, D. Rogińska, A. Sobuś, M. Wasilewska, Z. Ulańczyk and B. Machaliński, Novel design of (PEG-ylated)PAMAM-based nanoparticles for sustained delivery of BDNF to neurotoxin-injured differentiated neuroblastoma cells, *J. Nanobiotechnol.*, 2020, **18**(1), 120, DOI: **10.1186/s12951-020-00673-8**, PMID: 32867843; PMCID: PMC7457365.

26 Y. Zhu, M. Yue, T. Guo, F. Li, Z. Li, D. Yang and M. Lin, PEI-PEG-Coated Mesoporous Silica Nanoparticles Enhance the Antitumor Activity of Tanshinone IIA and Serve as a Gene Transfer Vector, *Evid Based Complement Alternat. Med.*, 2021, **2021**, 6756763, DOI: **10.1155/2021/6756763**, PMID: 34790248; PMCID: PMC8592735.

27 K. Qian, X. Bao, Y. Li, P. Wang, Q. Guo, P. Yang, S. Xu, F. Yu, R. Meng, Y. Cheng, D. Sheng, J. Cao, M. Xu, J. Wu, T. Wang, Y. Wang, Q. Xie, W. Lu and Q. Zhang, Cholinergic Neuron Targeting Nanosystem Delivering Hybrid Peptide for Combinatorial Mitochondrial Therapy in Alzheimer's Disease, *ACS Nano.*, 2022, **16**(7), 11455–11472, DOI: **10.1021/acsnano.2c05795**, Epub 2022 Jul 15, PMID: 35839463.

28 P. W. Gugu Nkosi, R. Chandran and H. Abrahamse, Hypocrellin: A Natural Photosensitizer and Nano-Formulation for Enhanced Molecular Targeting of PDT of Melanoma, *Wiley Interdiscip. Rev.: Nanomed. Nanobiotechnol.*, 2024, **16**(6), e1997, DOI: **10.1002/wnan.1997**, PMID: 39568119; PMCID: PMC11579242.

29 W. Wang, Z. Tang, Y. Zhang, Q. Wang, Z. Liang and X. Zeng, Mussel-Inspired Polydopamine: The Bridge for Targeting Drug Delivery System and Synergistic Cancer Treatment,

30 L. Wu, C. Wang and Y. Li, Iron oxide nanoparticle targeting mechanism and its application in tumor magnetic resonance imaging and therapy, *Nanomedicine*, 2022, **17**(21), 1567–1583, DOI: **10.2217/nnm-2022-0246**, Epub 2022 Dec 2, PMID: 36458585.

31 S. Geng, Q. Feng, C. Wang, Y. Li, J. Qin, M. Hou, J. Zhou, X. Pan, F. Xu, B. Fang, K. Wang and Z. Yu, A Versatile PDA(DOX) Nanoplatform for Chemo-Photothermal Synergistic Therapy against Breast Cancer and Attenuated Doxorubicin-Induced Cardiotoxicity, *J. Nanobiotechnol.*, 2023, **21**(1), 338, DOI: **10.1186/s12951-023-02072-1**, PMID: 37735669; PMCID: PMC10512561.

32 M. E. Lynge, P. Schattling and B. Städler, Recent developments in poly(dopamine)-based coatings for biomedical applications, *Nanomedicine*, 2015, **10**(17), 2725–2742, DOI: **10.2217/nnm.15.89**, Epub 2015 Sep 7, PMID: 26377046.

33 H. H. Ju, E. Kim, H. Y. Yang, Y. R. Nam, J. Wu and L. H. Low-Viscous, Dilute Phase Adhesive from Dense Polyphenolic Coacervates of Poly(vinyl alcohol) and Tannic acid, *ACS Omega*, 2023, **9**(2), 2953–2961, DOI: **10.1021/acsomega.3c08833**, PMID: 38250346; PMCID: PMC10795147.

34 Q. Chen, X. Shan and S. Shi, *et al.*, Tumor microenvironment-responsive polydopamine-based core/shell nanoplatform for synergetic theranostics, *J. Mater. Chem. B*, 2020, **8**(18), 4056–4066.

35 H. Zhang, Y. Sun, R. Huang, H. Cang, Z. Cai and B. Sun, pH-sensitive prodrug conjugated polydopamine for NIR-triggered synergistic chemo-photothermal therapy, *Eur. J. Pharm. Biopharm.*, 2018, **128**, 260–271, DOI: **10.1016/j.ejpb.2018.05.013**, Epub 2018 May 5, PMID: 29733952.

36 W. Cheng, C. Liang and L. Xu, *et al.*, TPGS-Functionalized Polydopamine-Modified Mesoporous Silica as Drug Nanocarriers for Enhanced Lung Cancer Chemotherapy against Multidrug Resistance, *Small*, 2017, **13**, 29.

37 M. Zhang, F. Zhang, T. Liu, P. Shao, L. Duan, J. Yan, X. Mu and J. Jiang, Polydopamine Nanoparticles Camouflaged by Stem Cell Membranes for Synergistic Chemo-Photothermal Therapy of Malignant Bone Tumors, *Int. J. Nanomed.*, 2020, **15**, 10183–10197, DOI: **10.2147/IJN.S282931**, PMID: 33363374; PMCID: PMC7754090.

38 W. Lei, C. Sun, T. Jiang, Y. Gao, Y. Yang, Q. Zhao and S. Wang, Polydopamine-coated mesoporous silica nanoparticles for multi-responsive drug delivery and combined chemo-photothermal therapy, *Mater. Sci. Eng., C*, 2019, **105**, 110103, DOI: **10.1016/j.msec.2019.110103**, Epub 2019 Aug 22, PMID: 31546357.

39 Y. Li, C. Jiang, D. Zhang, Y. Wang, X. Ren, K. Ai, X. Chen and L. Lu, Targeted polydopamine nanoparticles enable photoacoustic imaging guided chemo-photothermal synergistic therapy of tumor, *Acta Biomater.*, 2017, **47**, 124–134, DOI: **10.1016/j.actbio.2016.10.010**, Epub 2016 Oct 6, PMID: 27721008.

40 H. Wu, M. Wei, Y. Xu, Y. Li, X. Zhai, P. Su, Q. Ma and H. Zhang, PDA-Based Drug Delivery Nanosystems: A Potential Approach for Glioma Treatment, *Int. J. Nanomed.*, 2022, **17**,

Macromol. Biosci., 2020, **20**(10), e2000222, DOI: **10.1002/mabi.202000222**, Epub 2020 Aug 6, PMID: 32761887.

3751–3775, DOI: **10.2147/IJN.S378217**, PMID: 36065287; PMCID: PMC9440714.

41 J. Liao, H. Zhang and X. Wang, Polydopamine-doped virus-like mesoporous silica coated reduced graphene oxide nanosheets for chemo-photothermal synergetic therapy, *J. Biomater. Appl.*, 2020, **35**(1), 28–38, DOI: **10.1177/0885328220916968**, Epub 2020 Apr 11, PMID: 32279577.

42 L. Sun, P. Zhao and M. Chen, *et al.*, Taxanes prodrug-based nanomedicines for cancer therapy, *J. Controlled Release*, 2022, **348**, 672–691.

43 A. Sakai, Y. Yamashita, S. Misumi, N. Kishimoto, R. Onodera, T. Higashi, H. Arima and K. Motoyama, Nanoparticles of folic acid-methyl-β-cyclodextrin (FA-MβCD)/adamantane-albumin exhibit enhanced antitumor activity compared with FA-MβCD alone, *FEBS Open Bio*, 2023, **13**(2), 233–245, DOI: **10.1002/2211-5463.13540**, Epub 2022 Dec 26, PMID: 36537756; PMCID: PMC9900082.

44 Y. Chen, F. Zhang, Q. Wang, H. Lin, R. Tong, N. An and F. Qu, The synthesis of LA-Fe3O4@PDA-PEG-DOX for photothermal therapy-chemotherapy, *Dalton Trans.*, 2018, **47**(7), 2435–2443, DOI: **10.1039/c7dt04080f**, PMID: 29379913.

45 F. Wang, N. Li, W. Wang, L. Ma, Y. Sun, H. Wang, J. Zhan and D. Yu, A Multifunctional, Highly Biocompatible, and Double-Triggering Caramelized Nanotheranostic System Loaded with Fe3O4 and DOX for Combined Chemo-Photothermal Therapy and Real-Time Magnetic Resonance Imaging Monitoring of Triple Negative Breast Cancer, *Int. J. Nanomed.*, 2023, **18**, 881–897, DOI: **10.2147/IJN.S393507**, PMID: 36844435; PMCID: PMC9948638.

46 X. Fan, Z. Yuan, C. Shou, G. Fan, H. Wang, F. Gao, Y. Rui, K. Xu and P. Yin, cRGD-Conjugated Fe3O4@PDA-DOX Multifunctional Nanocomposites for MRI and Antitumor Chemo-Photothermal Therapy, *Int. J. Nanomed.*, 2019, **14**, 9631–9645, DOI: **10.2147/IJN.S222797**, PMID: 31824156; PMCID: PMC6901060.

47 X. Mu, F. Zhang, C. Kong, H. Zhang, W. Zhang, R. Ge, Y. Liu and J. Jiang, EGFR-targeted delivery of DOX-loaded Fe3O4@polydopamine multifunctional nanocomposites for MRI and antitumor chemo-photothermal therapy, *Int. J. Nanomed.*, 2017, **12**, 2899–2911, DOI: **10.2147/ijn.s131418**, PMID: 28435266; PMCID: PMC5391832.

48 F. Y. Liu, X. X. He and Z. Lei, *et al.*, Facile preparation of doxorubicin-loaded upconversion@polydopamine nanoplatforms for simultaneous in vivo multimodality imaging and chemophotothermal synergistic therapy, *Adv. Healthcare Mater.*, 2015, **4**(4), 559–568.